

Influence of the ionization rate of a plasma discharge applied to the modification of a supersonic low Reynolds number flow field around a cylinder

V Lago¹, R Jousset¹ and J-D Parisse²

¹ ICARE, CNRS, UPR 3021, 1C Avenue de la Recherche Scientifique, 45071, Orléans Cedex 2, France

² IUSTI, Aix Marseille Université / CNRS, UMR 7343, 5 rue Enrico Fermi, Technopôle Château-Gombert, 13453, Marseille Cedex 13, France

E-mail: viviana.lago@cnrs-orleans.fr

Abstract. This paper describes experimental and numerical investigations focused on the shock wave modification induced by a plasma actuator in rarefied flow regime. The experimental investigation was carried out in the supersonic wind tunnel MARHy located at the ICARE laboratory, and the numerical investigation using a 2D fully compressible Navier Stokes simulation was carried out at the IUSTI laboratory. The study concerns a cylinder in a Mach 2 air flow equipped with a small electrode that creates a local plasma. Electrical and optical diagnostics were used to experimentally analyze the plasma effects on the flow field. Measurements show that the shock stand-off distance increases with the discharge power. Numerical simulations show that the modification of the shock position is not induced by thermal effects. A theoretical approach is then developed in order to take into account the specific properties of plasma such as thermal non-equilibrium and ionization. It is found that the stand-off distance is directly coupled with the ionization degree of the plasma.

PACS numbers: 47.40.Ki, 52.80.-s, 47.85.L-, 52.77.-j

Submitted to: *J. Phys. D: Appl. Phys.*

1. Introduction

In recent years, the numerous reviews available in the literature testify to the growing interest in using weakly ionized gases in order to perform active flow control from subsonic to supersonic, and even hypersonic, flow regimes. The reader is referred to Semenov *et al* [1], Fomin *et al* [2], Bletzinger *et al* [3], Moreau *et al* [4], Corke *et al* [5], Cattafesta and Sheplak [6], and Wang *et al* [7]. Weakly ionized gases can be used to control flows when the abilities of traditional methods are close to natural limitations (e.g., due to a strict localization and slow time response). Electrohydrodynamic (EHD) technologies have therefore been considered to increase flow control effectiveness thanks to their interesting properties such as total electric control, no moving parts and fast response time.

In supersonic and hypersonic flow regimes the main problem is associated with the generation of shock waves resulting in high mechanical and thermal loads on aircraft, a sharp rise in drag force, and a reduction in the efficiency of the propulsion device. For supersonic and hypersonic vehicle designers, plasma actuators are good candidates to reduce wave and viscous drags and heat fluxes, to increase lift, to mitigate sonic boom and to control the boundary layer, turbulent transition or shock wave propagation. However, although extensive research has been undertaken in the past few decades, the plasma effects responsible for flow modifications are still not well understood and remain a controversial issue (e.g., [8]). Several features have given rise to speculation. The most popular issue is the anomalous shock stand-off distance of a body (generally a sphere) flowing supersonically in a weakly ionized plasma. It was observed experimentally for the first time in the 1970s by Russian researchers [9] who reported several experiments in which a thermal-only effect was not sufficient to explain the flow modification [2, 3].

The anomalous plasma effect results in an higher shock stand-off distance in a plasma than in an un-ionized gas heated up to the plasma temperature and at the same flow velocity [9]. Thus, it appears that the heat release of the plasma, due to Joule heating or thermal non-uniformities, is not the only mechanism which modifies the flow field around the body. Some authors introduced concurrent mechanisms to explain the flow modifications observed. For instance, Samimy *et al* [10] proposed that the local pressure increase produced by the gas heating acts like a solid obstacle such as a tab suddenly placed in the flow. Other studies (Leonov *et al* [11, 12], Klimov *et al* [13], Bityurin *et al* [14]) suggested that the plasma generation differs from conventional heating since the plasma structure is itself sustained by the flow structure: the influence of the plasma over the flow can then lead to unforeseeable consequences. One of the explanations put forward is vibrational-translation relaxation (V-T) due to non-thermal mechanisms in the plasma. In this case the area of power deposition is not equal to the area of temperature increase. Plasma discharges appear to induce heating of the gas, thus increasing the local sound speed and reducing the gas density, which leads to observed modifications in the flow.

The present work focuses on the modification of the shock position upstream a

circular cylinder in a rarefied Mach 2 air flow with a plasma actuator. The Mach number is defined as the ratio of the local velocity to the local sound speed ($M = v/c$). As the basic phenomena associated with this geometry are relatively well known, the contribution of the plasma to the flow modification should be easier to comprehend. The detached bow shock present ahead of the body is pushed upstream when the plasma is present. A negative glow discharge is created with a metallic electrode placed on the cylinder surface and connected to a dc high voltage power supply. Numerical and experimental investigations were performed and are compared in the present paper, for a set of plasma discharge conditions.

The authors have in previous works investigated the plasma actuator effects over a flat plate with similar flow conditions [15, 16]. In the case of a flat plate, the plasma properties involved in flow modifications were different from those presented in this work. With the flat plate geometry, the shock wave is created by the boundary layer, developing above the plate. It was experimentally and numerically demonstrated that the surface heating of the flat plate is responsible of an increase in the boundary layer thickness, pushing up the shock wave (i.e. the shock angle increases). With a circular cylinder, the shock wave is created by the model geometry itself. Thus, even if the heating can impact on the gas viscosity, and therefore the associated boundary layer, one can expect that this type of actuation could have a minor role on the modification of the shock wave position when the plasma actuator is switched on.

The application field of our investigations concerns the reentry vehicles (lifting- or winged-type) [17, 18]. For example, in the case of a lifting vehicle, a lifting body arrangement is used with no wing of any sort and movable flaps for aerodynamic control (for instance, see the IXV, Intermediate eXperimental Vehicle, developed by the European Space Agency [19, 20]). In future designs of lifting reentry vehicles, one might think to replace the flaps or part of them by plasma actuator systems [21] in order to allow the aerodynamic control of the vehicle, reduce the weight of the vehicle and solve some problems of heat load.

2. Experimental setup

2.1. The MARHy wind tunnel

The MARHy low density facility (formerly known as SR3 [22], Lab. Aérothermique) is currently used both for academic and industrial research. A schematic view of the facility is presented in figure 1. It consists of three parts: the settling chamber with a diameter of 1.3 m and a length of 2.0 m, the test chamber with a diameter of 2.3 m and a length of 5.0 m, and a third chamber in which a diffuser is installed. The diffuser is connected to the pumping group by a vacuum gate. A powerful pumping group with 2 primary pumps, 2 intermediary Roots and 12 Roots ensures in continuous operating mode the low density flow conditions. Depending on the desired rarefaction level, the number of pumps used can be chosen.

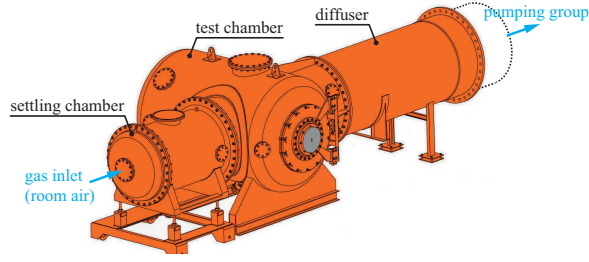


Figure 1. Schematic view of the MARHy facility.

When supplied with different nozzles, the wind tunnel generates subsonic, supersonic and hypersonic flows from Mach 0.6 to Mach 22, and covers a large range of Reynolds numbers from 10^2 up to 10^5 . Figure 2 shows the working conditions domain of the MARHy facility where the Reynolds numbers are based on a model length of 10 cm. The present study was carried out with a contoured Mach 2 nozzle (Reynolds number of 810 in figure 2), giving a uniform flow distribution through the test section with a core 12 cm in diameter [16]. The nominal operating conditions are summarized in table 1. The pressure in the test section corresponds to a geometric altitude of 67 km [23].

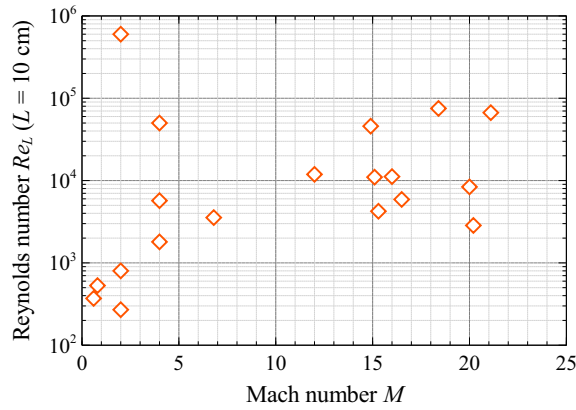


Figure 2. Mach-Reynolds diagram for the MARHy wind tunnel.

Table 1. Operating conditions.

Stagnation conditions	Flow conditions
$p_{st} = 63 \text{ Pa}$	$p_0 = 8 \text{ Pa}$
$T_{st} = 300 \text{ K}$	$T_0 = 163 \text{ K}$
$\rho_{st} = 7.44 \times 10^{-4} \text{ kg}\cdot\text{m}^{-3}$	$\rho_0 = 1.71 \times 10^{-4} \text{ kg}\cdot\text{m}^{-3}$
	$\mu_0 = 1.10 \times 10^{-5} \text{ Pa}\cdot\text{s}$
	$v_0 = 511 \text{ m}\cdot\text{s}^{-1}$
	$M_0 = 2$
	$\lambda_0 = 0.375 \text{ mm}$
	$q_m = 3.34 \times 10^{-3} \text{ kg}\cdot\text{s}^{-1}$

2.2. The cylinder-discharge setup

The model under investigation is a circular cylinder made of alumina, with a diameter of $D_{cyl} = 20$ mm and a spanwise length of 80 mm (figure 3). An aluminum electrode is flush mounted on the cylinder in the spanwise direction. It is 0.5 mm thick, 75 mm long, and 3 mm wide. The cylinder is mounted in the test section, 174 mm downstream the nozzle exit, with its longitudinal axis perpendicular to the main flow direction. For these cylinder dimensions and experimental conditions, the Reynolds number is around 160. The plasma is produced with a glow discharge generated by connecting the electrode to a high voltage dc power supply (Spellman SR15PN6) through a resistor ($R_s = 10.6$ k Ω). The electrode is negatively biased compared to the rest of the device (i.e., the wind tunnel metallic parts) which is grounded and collects negative charges from the plasma, ensuring the current looping. The voltage V_s is fixed with the power supply, which delivers the discharge current I_{HV} . The voltage applied to the electrode (V_{HV}) is then calculated with the following relation: $V_{HV} = V_s - R_s I_{HV}$. The discharge is ignited in ambient air.

2.3. Optical diagnostics

The flow around the cylinder ionized by the plasma discharge is analyzed by means of optical diagnostics. The light is collected through a quartz window located in the wall of the test section chamber (see Menier *et al* [15] for further details on the optical arrangement). A PI Max Gen-II ICCD camera equipped with a VUV objective lens (94 mm, F/4.1) was used to observe the influence of the plasma discharge on the flow around the cylinder.

The spectroscopy measurements were carried out with an Ebert-Fastie-type monochromator SOPRA F1500. It has a focal length of 1500 mm and a grating of 1800 grooves/mm. The plasma is imaged onto the monochromator by two plano-convex lens connected to the entrance slit by a quartz optical fiber. The detector is an intensified array of 1024 pixels (Princeton Instruments IRY 1024) scanning with an 8.5 nm wavelength range. The OMA is cooled by a Peltier element, which gives an operating temperature of -35 °C.

3. Numerical approach

Investigations involved in this work concerns supersonic flows in rarefied regime. The Knudsen number ($Kn = \lambda/D_{cyl}$) calculated with the input parameters of the experimental inflow conditions (Table 1) is $Kn = 0.019$, corresponding to the slip-flow regime (slightly rarefied) [24]. Such type of flows can be simulated using Direct Monte Carlo method, as illustrated by the literature (for instance, [25–27]). However, others authors (for instance, [28, 29]) have developed models to adapt classical approaches applied for high Knudsen number to cases for what $Kn \ll 1$. In the present work, this last type of approach is used. The 2D compressible Navier-Stokes simulations are

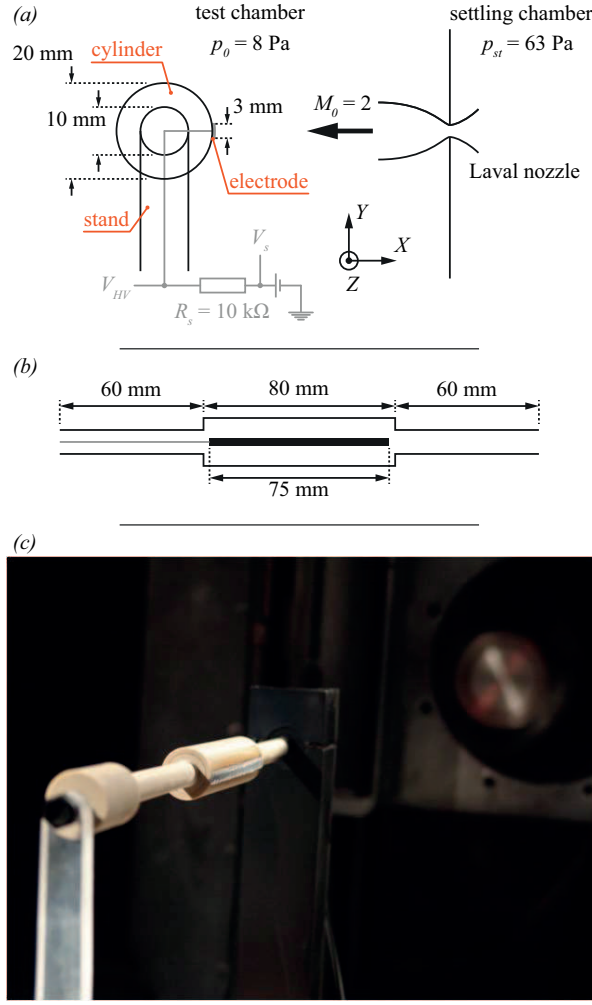


Figure 3. Schematic representation of the cylinder: (a) side and (b) front views, and (c) picture of the cylinder placed inside the test section.

performed by adapting the boundary conditions (see section 3.2) to match with the physical phenomena involved in a rarefied flow regime.

The numerical code uses a structured grid based on the discretization of the unsteady compressible Navier-Stokes equations by an explicit cell-centered finite volume method. The convective block (Euler) is discretized using a WENO third order accurate TVD-upwind, cell-centered finite volume scheme. The associated Riemann solver is HLLC. The diffusive block is then discretized with a finite difference scheme. Temporal integration is performed by a 2nd-order Runge-Kutta procedure. This code has been validated on numerous test cases and especially for supersonic rarefied flows [30].

3.1. Governing Equations

In order to describe the air flow, the 2D full compressible Navier-Stokes equations are used in the conservative form, with:

- the continuity equation :

$$\frac{\partial \rho}{\partial t} + \frac{\partial \rho u_i}{\partial x_i} = 0, \quad (1)$$

where x_i is the space coordinate, t is the time, ρ is the density, and u_i is the velocity in the space direction x_i .

- the momentum conservation equation :

$$\frac{\partial \rho u_j}{\partial t} + \frac{\partial (\rho u_j u_i + p \delta_{ij} - \tau_{ij})}{\partial x_i} = 0, \quad (2)$$

where p is the pressure, τ_{ij} is the viscous shear stress tensor, and δ_{ij} is Kronecker's symbol. We assume that the fluid is Newtonian, so the viscous shear stress tensor can be written as:

$$\tau_{ij} = \mu \left(\frac{\partial u_i}{\partial x_j} + \frac{\partial u_j}{\partial x_i} \right) - \delta_{ij} \frac{2}{3} \mu \frac{\partial u_k}{\partial x_k}, \quad (3)$$

where μ is the viscosity coefficient [31, 32].

- the energy conservation equation:

$$\frac{\partial \rho e_t}{\partial t} + \frac{\partial (\rho u_i e_t + u_i p - u_i \tau_{ij} + q_i)}{\partial x_i} = 0, \quad (4)$$

where $e_t = e + (\rho \Sigma u_i^2) / 2$ is the total energy, e is the internal energy, and q_i is the heat flux in the space direction i . The Prandtl number is 0.7, corresponding to air gas.

3.2. Boundary Conditions

Because of the rarefied regime, the boundary conditions applied in the equation system (1)–(4) are the slip velocity and the temperature jump conditions on the solid wall (denoted with the subscript $_w$). Taking into consideration the first-order Knudsen number conditions, the complete slip boundary condition can be written as follows [33]:

$$u_s = -\sigma_p \frac{\mu}{p} v_m \left(\frac{\partial u}{\partial y} \right)_w + \sigma_T \frac{\mu}{\rho} \left(\frac{\partial \ln T}{\partial x} \right)_w, \quad (5)$$

where $v_m = \sqrt{2\mathcal{R}T_w(x)}$ is the most probable molecular velocity at the surface temperature T_w , σ_p is the slip velocity coefficient, \mathcal{R} is the ideal gas constant, and σ_T is the thermal slip coefficient. In this work we apply the velocity slip coefficient $\sigma_p = 1.012$ given in [33], under the full accommodation assumption. Concerning the thermal slip coefficient σ_T numerous theoretical data are summarized in [34]. In the present study the second term in equation (5) was not taken into account because there is one order of magnitude difference compared to the first term, even if the surface temperature gradient in the x direction is taken into account.

The boundary condition proposed by Kogan (eq. 2.7a in [33]) was chosen to describe the temperature jump at the wall, using a temperature jump coefficient. A first expression of this coefficient was proposed by von Smoluchowski [35] and then

Kennard [36], but in this study we use the expression proposed by Kogan [33], taking into consideration the diffuse reflection assumption and the Knudsen layer effect. Similar values of the temperature jump coefficient are proposed in [37] and the mean free path is calculated using the variable hard sphere model (VHS) proposed by Bird [38].

3.3. Mesh and time step

The computational domain is divided into 8 blocks for parallel computing purposes, with a total number of $600 \times 248 = 148\,800$ cells. The minimum space step ($\Delta_{x_{min}} = 5 \times 10^{-4}$ m), was chosen as a result of the convergence study and also taking into account the mean free path value in the free stream (table 1). The CFL coefficient used to carry out simulations was 0.75.

In order to simulate the discharge interaction with the flow, two different thermal effects induced by the plasma discharge were simulated separately. On the one hand, the surface heating of the electrode was considered by fixing two temperatures for the Dirichlet boundary condition on the cylinder wall: $T_{w_1} = 500$ K or 1000 K at the electrode position, and $T_{w_2} = 163$ K for the rest of the cylinder surface. T_{w_2} was also taken as the free stream temperature. On the other hand, a volumetric heating was simulated by adding a volumetric heating Q_v in the region between the cylinder and the shock in order to heat the flow here, whereas the initial temperature of the rest of the domain was set to T_{w_2} .

4. Results

4.1. The natural shock wave

The flow field around the cylinder was first investigated without the discharge (i.e., the plasma actuator was switched off). The shock wave shape and the shock stand-off distance Δ were experimentally visualized with the afterglow technique. This technique allows the shock wave to be visualized in low density flows [39]. The afterglow method consists of the ionization of the air in the vacuum chamber with a plane-to-plane dc discharge. In this study, a voltage was applied between two parallel rectangular copper plates separated by a gap of about 300 mm. The cylinder was placed between these plates, leading to a flow field of ionized air around the cylinder. The consecutive diffuse light emission was then focused on a camera. Due to air density variations in the shock, the light intensity variations in the resulting picture let the shock wave appear. Figure 4 shows the natural flow around the cylinder visualized with the ICCD camera (figure 4(a)) and with a Pentax K10D digital SLR camera (figure 4(b)). The air flows from the right to the left, as on every other following figure.

The shock wave is readily recognized on the images captured with the ICCD camera, enabling the estimation of the stand-off distance. In our conditions, the shape of the natural shock wave is hyperbolic and can be described by the following equation based on the Billig formulation [40]:

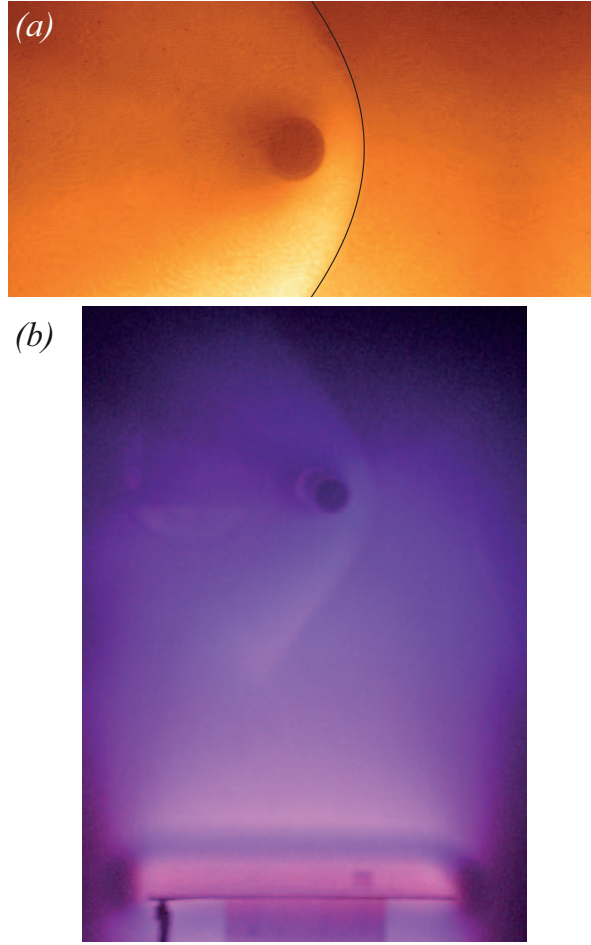


Figure 4. Images of the flow field around the cylinder without the discharge: (a) ICCD image (exposure time: 300 ms) and (b) digital camera image obtained with the afterglow technique.

$$x = R_{cyl} + \Delta - \frac{\varepsilon R_c}{\tan^2 \theta} \left[\left(1 + \frac{y^2 \tan^2 \theta}{\varepsilon R_c^2} \right)^{1/2} - 1 \right], \quad (6)$$

where x and y are the shock coordinates in the Cartesian coordinate system (centered on the cylinder center), R is the radius of the cylinder, R_c is the vertex radius of curvature (at $y = 0$), and $\theta = \arcsin M^{-1}$ is the angle of the hyperbola asymptote (i.e., the Mach angle). Coefficient ε is an adjustment parameter used to modify the hyperbola equation in order to match the shock wave shape observed on the ICCD images. In our conditions (a Mach 2 flow and a 20 mm-diameter cylinder), R_c was calculated with the correlation given by Ambrosio and Wortman [41] and is 83.9 mm. The adjustment parameter is $\varepsilon = 0.65$.

Determination of the shock stand-off distance results from the post processing of several ICCD images in order to distinguish the shock wave position more precisely than is possible from the raw image (contrast enhanced with ImageJ software [42]). For the

natural shock wave, Δ is estimated at $12.45 \text{ mm} \pm 0.10 \text{ mm}$. This experimental value is in good agreement with the one found by applying the following empirical formulation, with $R_{cyl} = 10 \text{ mm}$ and $M_0 = 2$:

$$\frac{\Delta}{R_{cyl}} = 0.386 \exp\left(\frac{4.67}{M_0^2}\right). \quad (7)$$

Equation (7) was proposed by Ambrosio and Wortman [41], and results from a correlation of experimental data for supersonic and hypersonic flow around a circular cylinder. In our flow conditions, the theoretical value of the stand-off distance obtained with (7) is $\Delta_0 = 12.41 \text{ mm}$. In addition, it can be seen that, even if the contrast of the raw image is low, the three dark zones with a trident-like shape are present in the cylinder wake. They correspond to three lower density zones. The first one is aligned along the flow direction and corresponds to the wake of the cylinder where the velocity is low. The other two zones are slanted and located in a zone where the velocity is higher, inducing a decrease in the density.

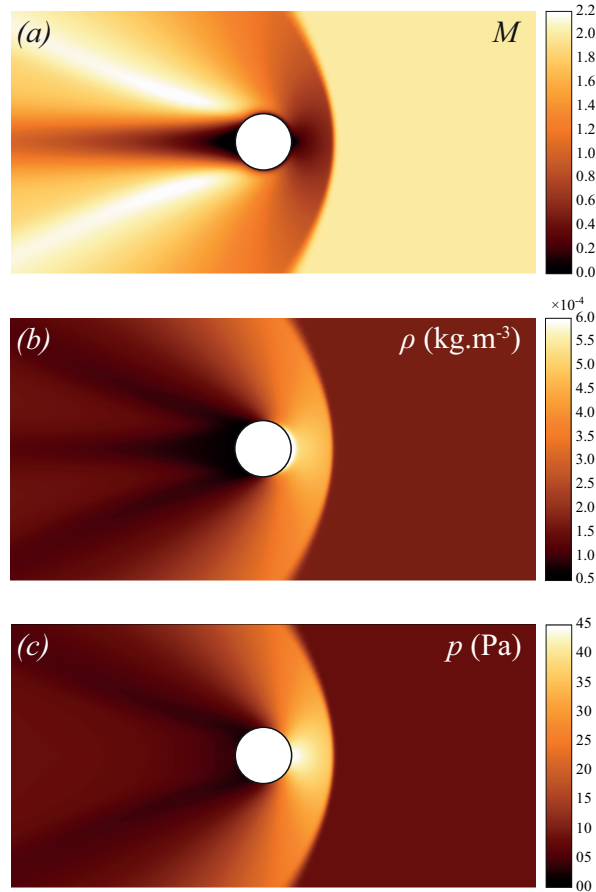


Figure 5. Results from the WENO simulation of the natural flow: (a) Mach, (b) density, and (c) pressure fields. The free stream Mach number is 2.

The numerical simulation of the Mach 2 flow field around the cylinder was calculated

with the WENO code described above. This simulation was run with input parameters corresponding to the experimental inflow conditions (table 1). The resulting Mach number and density flow fields are shown in figure 5. The detachment shock distance was determined from the density field. The shock stand-off distance obtained was 13.71 mm which is slightly larger than the experimental value found above ($\Delta = 12.45$ mm). Nevertheless the global shape is well reproduced and especially the wake flow field, since the three low density zones appear distinctively.

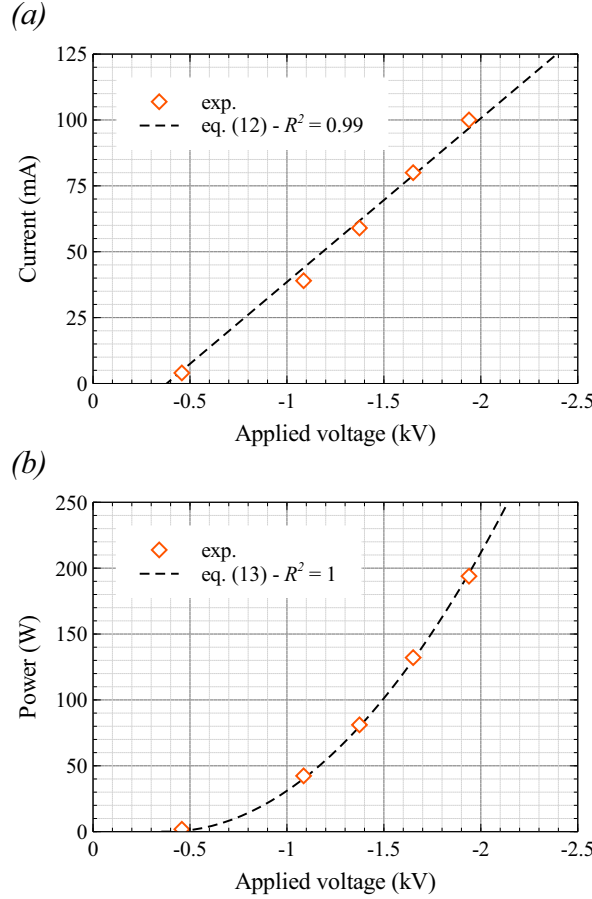


Figure 6. Electrical characterization of the discharge in a Mach 2 flow: (a) current-voltage characteristic and (b) power consumption versus the applied voltage.

4.2. Modification of the shock wave shape by the plasma discharge

4.2.1. Electrical characteristics and temperature estimation of the discharge The discharge was obtained by applying a negative dc potential to the electrode. The current-voltage characteristic and the power are plotted in figures 6(a) and 6(b), respectively. In our experimental conditions, the discharge ignites at around $V_{ign} = -0.38$ kV, and can be sustained down to around -2.5 kV. In this range, the discharge current I_{HV} (mA) increases linearly with the applied voltage V_{HV} (kV), as:

$$I_{HV} = -62.12 (V_{HV} - V_{ign}). \quad (8)$$

This behavior corresponds to an abnormal glow discharge regime [43]. Since the current is linearly linked to the applied voltage, the power P_{el} (W) evolved with V_{HV}^2 , as follows:

$$P_{el} = 80.67 (V_{HV} - V_{ign})^2. \quad (9)$$

These two laws are obtained by fitting (least-squares method) the experimental data.

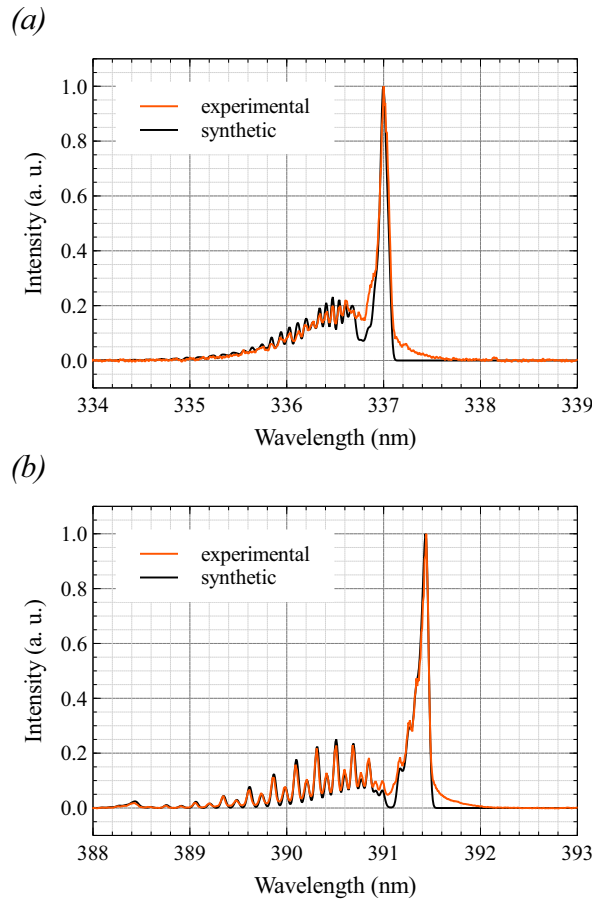


Figure 7. Experimental (with flow, $V_{HV} = -1.1$ kV) and synthetic spectra of: (a) N₂ spectral band at 337.1 nm and (b) N₂⁺ spectral band at 391.4 nm.

In order to estimate the temperature in the region affected by the discharge, the macroscopic temperature of the gas was deduced from the rotational temperature measured in the plasma region between the shock and the electrode. This method implies that the gap between the rotational and translational temperatures is negligible. This assumption has been verified for our experimental conditions [44]. The measurements were made 1 mm upstream the cylinder. Two nitrogen systems were observed: the

N_2^+ first negative system ($B^2\Sigma_u^+ \rightarrow X^2\Sigma_g^+$) and the N_2 second positive system ($C^3\Pi_u \rightarrow B^3\Pi_g$) at 3.16 eV and 11.05 eV [45], respectively. The emission spectra of neutral (N_2) and ionized (N_2^+) nitrogen molecular species were analyzed and compared to simulated spectra. Samples of the observed molecular bands are shown in figures 7(a) and 7(b).

The simulations were performed using a home-made code detailed in Lago [46]. A least-square curve fitting algorithm was used to optimize the experimental spectra by minimizing the deviation of the experimental data from the spectral values calculated as a function of the rotational and vibrational temperatures. The accuracy of this method is estimated to 5%. The results from best fit to the data are superimposed on the experimental data as shown in figure 7. The N_2 and N_2^+ rotational temperatures are plotted as a function of the applied discharge voltage in figure 8. In the case when the flow is operating, analysis of the rotational temperature behavior gives rise to three major observations:

- A thermal non-equilibrium is observed between the N_2 and the ionized species N_2^+ . The N_2 rotational temperature ranges between 350 K and 400 K whereas a lower rotational temperature is measured for N_2^+ (slightly below 300 K).
- These low temperature values (< 400 K) are measured 1 mm upstream the electrode. This position is expected to be close to the one where the rotational temperature is the highest. The temperature distribution across the region between the cylinder and the shock is assumed to be non-uniform. However, the temperature ranges between close levels, meaning its distribution has a minor influence on the shock wave.
- The rotational temperature values are constant with the applied voltage, especially below -0.8 kV. This particular feature for the ionized species N_2^+ shows that the energy supplied to the discharge is not stored as internal energy by the gas.

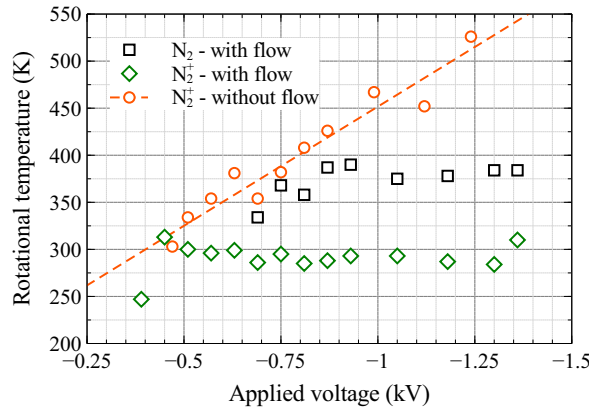


Figure 8. Comparison between N_2 and N_2^+ rotational temperatures, with flow ($M = 2$) and without flow versus the applied voltage.

To support this assumption, spectroscopy measurements were done without the Mach 2 flow and with a stagnation pressure of 8 Pa in the test chamber. In this case,

the rotational temperature increases linearly with the applied voltage from 303 K to 526 K, showing that the flow impacts strongly on the mechanisms of energy storage. These results are similar to those found with a flat plate configuration and published in Menier *et al* [15].

4.2.2. Modification of the stand-off distance With the discharge switched on, the afterglow technique was not used since the bright visible emission of the discharge itself allows visualization of the flow around the cylinder and the shock wave. Spectral analysis showed that the light emission arises from the first negative system of N_2^+ and above all from the second positive system of N_2 . No other molecular and atomic emission was observed, suggesting that the kinetic process of populations can be neglected. Furthermore the nitrogen excited electronic levels are strongly coupled with the ground state vibrational levels that relax extremely slowly. To confirm this assumption, the N_2 vibrational relaxation time calculated from Macheret *et al* [47] is plotted according to the temperature for different pressure conditions (figure 9). The pressure values correspond to the pressure in the test chamber (8 Pa), and to the pressure range (26 Pa–44 Pa) in the region between the cylinder and the shock wave estimated with the simulated pressure field (figure 5(c)). In addition, the N_2 vibrational relaxation length scale, calculated with a flow velocity of $511 \text{ m}\cdot\text{s}^{-1}$ is also reported in figure 9.

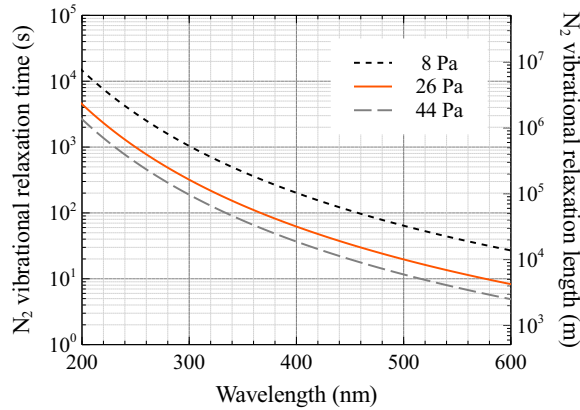


Figure 9. N_2 vibrational relaxation time and length according to the gas temperature for different pressure conditions. The curves were computed with expressions given by Macheret *et al* [47].

For a gas temperature ranging from 200 K to 600 K, the N_2 vibrational relaxation length has an order of magnitude varying from 10^7 m at low temperature to 10^4 m at high temperature. For an electronic temperature of 1 eV, the relaxation length corresponds to a few meters. In terms of time, the N_2 vibrational relaxation ranges between 1000 s and 10 s, which can be compared to the residence time of the flow (2 ms for 1 m). So, we can consider that the emission intensity reflects the modifications in both the flow and the shock wave.

Figure 10 shows the ICCD images of the shock wave modified by the discharge. The

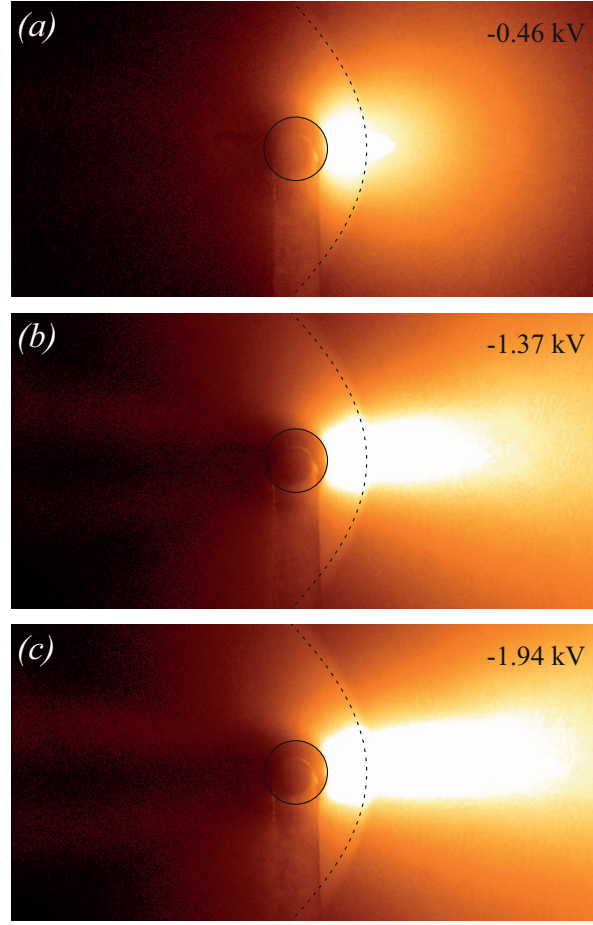


Figure 10. ICCD images of the flow modified by the plasma discharge: (a) -0.46 kV and 4 mA, (b) -1.37 kV and 59 mA, and (c) -1.94 kV and 100 mA. The black line represents the non-modified shock wave shape (i.e., without the discharge).

natural shock wave shape is superimposed on each image to facilitate the comparison between the different cases. As can be observed, the plasma changes locally the shape of the shock, pushing it upstream the flow. The symmetrical shape is sustained, but the curvature of the shock is modified (visible far from the cylinder). Therefore the adjustment parameter ε of equation (6), which is sensitive to the shock shape, has to be decreased (0.65 to 0.50) in order to preserve the semi-empirical shock shape (6) aligned with the experimental shape observed on the ICCD images. The stand-off distance on the stagnation line is estimated for each electrical discharge configuration from the experimental images using the same post processing method as that applied in the natural case.

The evolution of the experimental stand-off distance Δ_{exp} with the applied voltage and the electric power is plotted in figure 11. It can be seen that the stand-off distance depends linearly on the applied voltage, and thus on the square root of the power. The higher the applied voltage (or the power), the higher the stand-off distance of the shock wave is. The following empirical laws describe the variation in the experimental

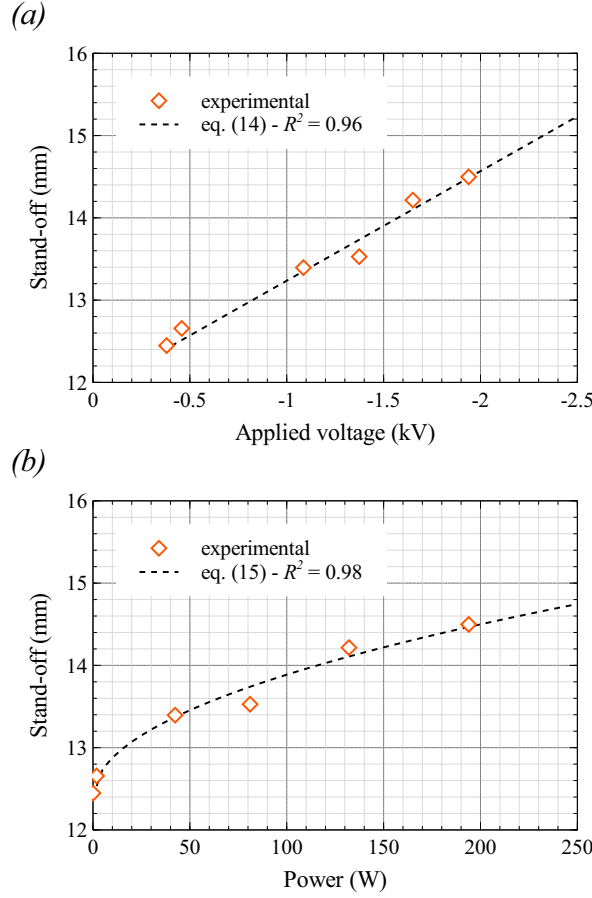


Figure 11. Experimental stand-off Δ_{exp} estimated with the ICCD images according to: (a) the applied voltage V_{HV} and (b) the power P_{el} . The lines represent the interpolation of experimental points with equations (10) and (11) respectively.

stand-off distance:

$$\Delta_{exp} = -1.33 (V_{HV} - V_{ign}) + \Delta_0, \quad (10)$$

and

$$\Delta_{exp} = 0.15 \sqrt{P_{el}} + \Delta_0, \quad (11)$$

where V_{HV} is expressed in kV, P_{el} in W, and the stand-off distances in mm (with $\Delta_0 = 12.41$ mm). The stand-off distance increases by $\delta\Delta = +1.7\%$ for an applied voltage of -0.46 kV till $+16.5\%$ for -1.94 kV.

5. Discussion

Hayes and Probstein [48] showed that the shock stand-off distance in front of a cylinder is a function of the density ratio across the shock wave as measured on the stagnation

streamline. In this study, the stand-off is increased when a plasma is created in the region between the cylinder and the shock wave. Thus, we can assume that the local flow properties behind the shock have been modified. Three types of effects can be considered in order to explain why the shock is pushed upstream: surface heating of the electrode, volumetric heating of the gas upstream the electrode where the plasma is present, and influence of the ionization degree. Each of these effects was tested separately in order to aid in discriminating between a thermal-only and a purely plasma effect.

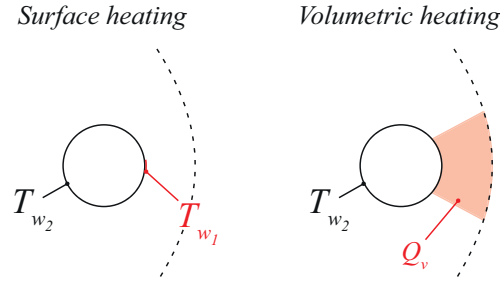


Figure 12. Scheme of the heating scenarios for the numerical simulations.

5.1. Surface heating simulations

In order to simulate the surface heating due to the ohmic heat effect induced by the electric power applied to the electrode, a number of cells on the cylinder perimeter corresponding to the electrode position were heated to a higher temperature than for the neutral case (figure 12). The cells located at the electrode position were set, and maintained during the calculation, at the temperature $T_{w_1} = 500$ K, and, in a second simulation, at $T_{w_1} = 1000$ K. In the second case, T_{w_1} was purposely set at an unacceptably high temperature for the electrode because the melting point of aluminum is about 933 K. Figure 13 shows the temperature and density fields calculated with the two electrode temperatures tested.

The shock stand-off distance determined from each case was 13.88 mm ($\delta\Delta = +1.24\%$) with $T_{w_1} = 500$ K and 14.48 mm ($\delta\Delta = +5.62\%$) with $T_{w_1} = 1000$ K, compared to $\Delta = 13.71$ mm for the natural shock simulated (see section 4.1). The obtained effect is far short of what was obtained experimentally. For the case with $T_{w_1} = 500$ K, the slight increase in Δ shows that surface heating is not able to reproduce an increase in the stand-off distance corresponding to that experimentally measured with the discharge on. In addition, the increase in Δ obtained with the temperature $T_{w_1} = 1000$ K, which is not physically consistent with the electrode material, is lower than that obtained for $V_{HV} < -1.1$ kV. In the case of a cylinder, the increase in the shock stand-off distance appears to be weakly linked to the surface heating process. It is an interesting result since it was shown in our previous study that the simulation of surface heating (with the same numerical code) correctly reproduces the effects of such

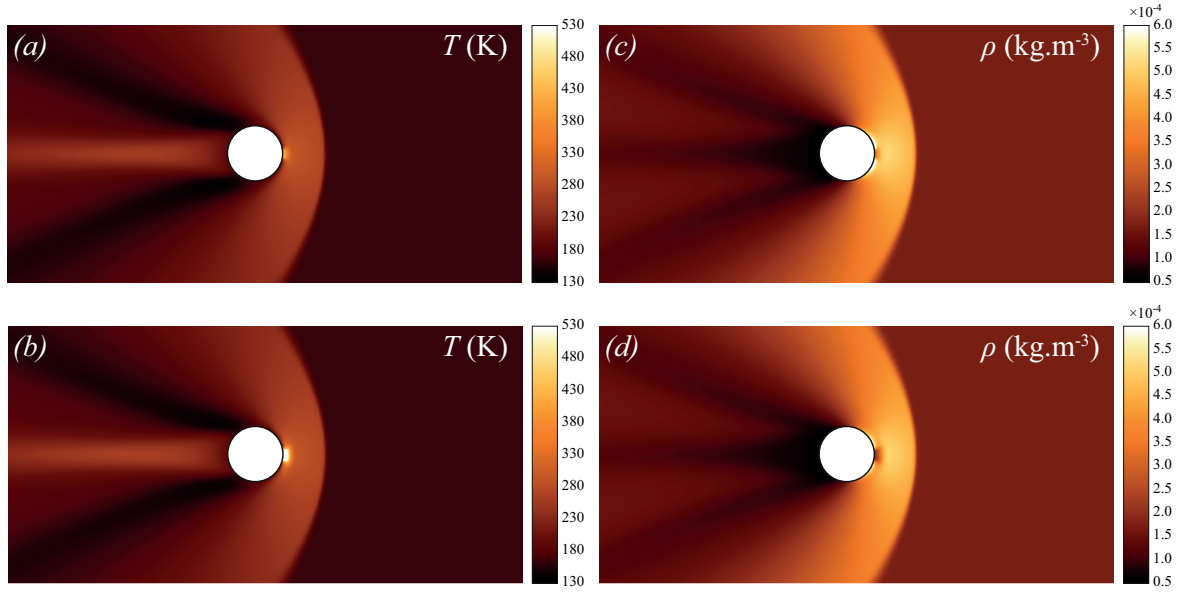


Figure 13. Results from the WENO simulation in the case of surface heating: (a)–(b) temperature fields for $T_{w1} = 500$ K and 1000 K respectively, and (c)–(d) density fields for $T_{w1} = 500$ K and 1000 K respectively. The free stream Mach number is 2.

a discharge on the flow over a flat plate [16]. In fact, we showed that in the case of a flat plate and with the same Mach 2 flow conditions, surface heating became preponderant and produced an increase in the shock angle.

For the present study, one can note that the temperature of the flow just behind the shock wave is weakly modified (figure 13(a)–(b)), leading to a slight increase in Δ . It is clear that the weakness of surface heating can be explained by the fact that Δ depends strongly on the state of the flow immediately behind the shock wave [49]. Volumetric heating was then considered in order to heat a larger region of the flow upstream the cylinder.

5.2. Volumetric heating simulations

In order to simulate the volumetric heating caused by the plasma between the cylinder and the shock, a region upstream the cylinder was heated by adding into the numerical code an energy equivalent to a volumetric heating of $Q_v = 15$ W (figure 12). To determine the number of cells defining the heated volume, the size of the plasma region was estimated from the experimental images. The numerical results are presented in figure 14.

The effectiveness of volume heating is presented in figure 14(a) with the calculated iso-temperature field, where it can be seen that volumetric heating is stronger close to the stagnation point (i.e., at the electrode position in the real case) than just behind the shock wave. For a volumetric heating of 15 W, the shock stand-off distance determined from the simulation increases by +34.9% ($\Delta = 18.50$ mm), which is a value over two

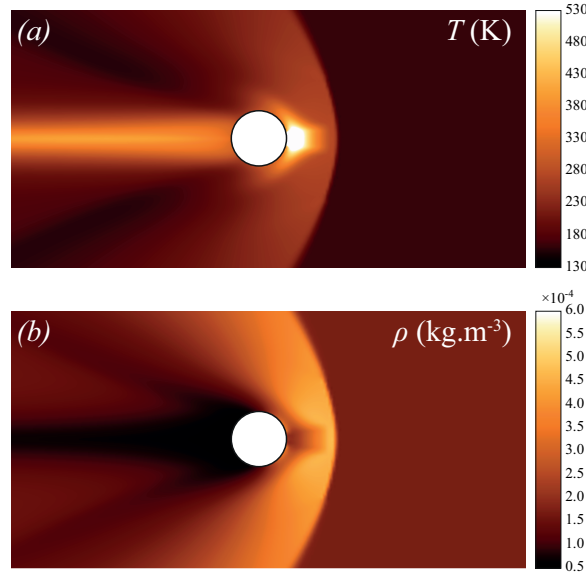


Figure 14. Results from the WENO simulation in the case of volumetric heating: (a) temperature and (b) Mach fields for a volumetric heating of $Q_v = 15$ W. The free stream Mach number is 2.

times greater than the value obtained with a discharge power of 190 W (+16.5%). In addition, the local temperature 1 mm upstream the cylinder surface can reach 700 K, which is inconsistent with the optical temperature measurements, since the temperature of the gas remains below 400 K (figure 8). The stand-off distance estimated with this numerical simulation is then unacceptably high with respect to the experimental values, meaning that the volumetric heating is not the dominant process when the discharge is switched on.

Both surface and volumetric heating are unable to simulate correctly the observed increase in the shock stand-off distance. This result has been indirectly reported by some authors. For instance, Lowry *et al* [50] measured an anomalous increase of the shock stand-off distance when they launched a spherical projectile into weakly ionized air. They showed that the temperature of the plasma appeared to be much lower than necessary to explain the measured Δ by thermal-only effects. In order to understand why the stand-off distance is increased beyond what can be attributed to thermal effects, the physical properties of the plasma must be considered.

5.3. Influence of the ionization rate

The shock stand-off distance is a function of the density ratio ρ_s/ρ_0 across the shock wave, which is a function of the ratio of specific heat γ [48]. The state of the flow behind the shock wave is therefore of great importance in explaining why Δ increased when the discharge was on. Schwartz and Eckerman [51] showed that the shock stand-off distance depends on the internal energy state immediately behind the shock wave. In addition, Mishin *et al* [9] confirmed experimentally that the shock stand-off distance from a sphere

is greater in a weakly ionized gas than in air heated to the plasma temperature. They explained their observations by the modification of the isentropic exponent inducing a modification in the speed of sound. The increase in the sound velocity in a weakly ionized plasma, according to the electron density (i.e., α_i), was first observed by Ishida *et al* [52]. Mishin [53] confirmed later that the sound velocity is modified because of the isentropic exponent, which is different in a weakly ionized gas from that in an un-ionized gas. A theoretical link between the properties of the plasma and the isentropic ratio was proposed by Burm *et al* [54] who shown the dependence of γ on the ionization degree α_i . In addition, they found that γ_* (the subscript $*$ stands for the plasma state) is always lower than that of the un-ionized gas. The modification in the speed of sound is induced by both an increase in the temperature of heavy particles in the plasma (i.e., the gas temperature) and a lower isentropic coefficient depending on the ionization degree.

In order to see how sensitive the shock stand-off distance is to the ionization degree in our experimental conditions, a modified version of the correlation (7) proposed by Ambrosio and Wortman [41] was used. If we assume that a normal shock wave is present on the stagnation streamline, the Mach number of the free stream M_0 can be expressed with the Mach number behind the shock M_1 and the isentropic exponent of the flow γ [55]:

$$M_0^2 = \frac{2 + (\gamma - 1) M_1^2}{2\gamma M_1^2 - (\gamma - 1)}. \quad (12)$$

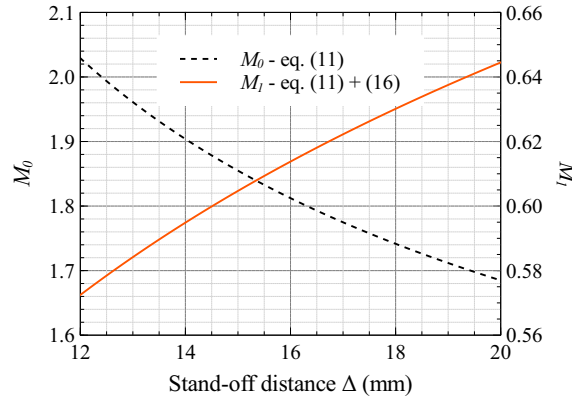


Figure 15. Mach numbers M_0 (upstream the shock wave) and M_1 (behind the shock wave) according to an artificial increase in the stand-off distance, calculated with the correlation (7).

Figure 15 shows the variations of M_0 and M_1 as a function of a theoretical increase in Δ , considering an air with $\gamma = 1.4$ and a constant temperature. This increase spans the one experimentally measured (section 4.2.2). One can observe that the Mach number upstream the shock wave, M_0 , decreases when Δ rises, with respect to the correlation (7). In turn, the Mach number downstream the shock wave, M_1 , is increased. The variation of M_0 depicted in figure 15 is consistent with the experimental observations summarized by Fomin *et al* [2] and Bletzinger *et al* [3]: the shock stand-off distance

in a plasma is always greater than the value found in an un-ionized gas (same static temperature and velocity) due to the lower flight Mach number (i.e., M_0) of the body. According to the results of figure 15, two scenarios can be followed to increase the stand-off distance: either change the properties of air upstream the shock in order to decrease M_0 , or modify the air properties downstream the shock to increase M_1 . In our experimental conditions, the most probable scenario to explain the greater values of Δ when the discharge is on is an increase in M_1 . Indeed, the plasma is created from the aluminum electrode, with its most luminous part between the cylinder and the shock wave, inducing a greater gas temperature (see section 4.2.1) and a lower exponent ratio [54].

Since the gas upstream the cylinder is weakly ionized when the discharge is switched on, correlation (7) can be expressed as a function of a Mach number behind the shock wave and an exponent ratio, both relative to the plasma:

$$\frac{\Delta^*}{R_{cyl}} = 0.386 \exp \left[4.67 \frac{2\gamma^* M_1^{*2} - (\gamma^* - 1)}{2 + (\gamma^* - 1) M_1^{*2}} \right], \quad (13)$$

where γ^* (14) is the isentropic exponent of a diatomic plasma in non-local thermodynamic equilibrium, given by Burm *et al* [54].

$$\gamma^* = \frac{c_p^*}{c_v^*} \frac{2\theta + (1 - \theta) \alpha_i}{2\theta + (1 - \theta) \alpha_i + (1 - \alpha_i) \alpha_i} \quad (14)$$

In equation (14), c_p^* and c_v^* are the heat capacities of the plasma (eq. (42) and (43) in [54], respectively), $\alpha_i = n_e/n_0$ is the ionization degree with n_e the electronic density and n_0 the neutral particle density, and $\theta = T_{gas}/T_e$ is the thermal disequilibrium between the gas temperature T_{gas} and the electronic temperature T_e . The heat capacities of the plasma are functions of the ionization energy, corresponding here to that of the predominant ionized species N_2^+ (15.7 eV [45]).

Figure 16 shows the theoretical variation of γ^* obtained with (14), according to an ionization degree ranging from 10^{-6} to 10^{-2} . The gas temperature was fixed at $T_{gas} = 375$ K (estimated with figure 8) and the electronic temperature was fixed at $T_e = 1$ eV. The isentropic exponent decreases from 1.4 (un-ionized gas) to about 1.12, and remains almost constant for higher ionization degrees. This value is slightly lower than the one considered by Burm *et al* [54] for common plasmas (1.16). It can be seen that the isentropic degree begins to decrease significantly for $\alpha_i > 10^{-5}$, which corroborates the hypothesis of Bletzinger *et al* [3] who argued that for a very low ionization degree ($\approx 10^{-7}$), the increase in the stand-off distance in an ionized gas is predominantly due to thermal effects.

If we consider that the gas velocity just behind the shock is weakly modified by the plasma, the relation between the Mach number M_1 without the discharge and the Mach number M_1^* with the plasma can be expressed as:

$$M_1 c_1 = M_1^* c_1^*, \quad (15)$$

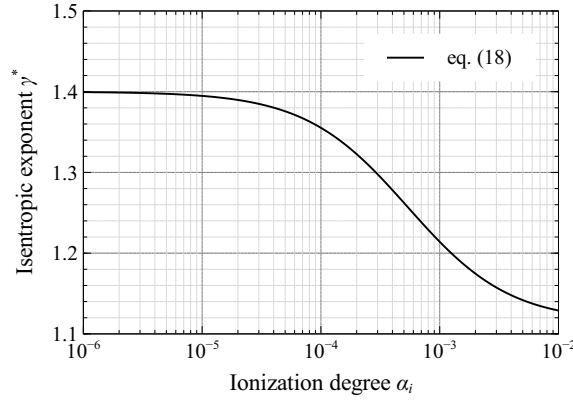


Figure 16. Isentropic exponent of the plasma according to the ionization degree, calculated with (14).

where $c_1 = (\gamma \mathcal{R} T_1)^{1/2}$ is the local speed of sound for an un-ionized gas, and c^* (16) is the sound velocity in a plasma, defined by Burm *et al* [56]. Given that the ratio between the temperature T_1 behind the shock wave for the natural flow and the temperature of the weakly ionized gas T_1^* is close to unity, and the flow conditions are $\gamma = 1.4$, $M_0 = 2$, and $M_1^2 = 1/3$ (calculated with (12)), expression (15) leads to (17).

$$c^* = [\gamma^* \mathcal{R} (T_1^* + \alpha_i T_e)]^{1/2} \quad (16)$$

$$M_1^{*2} = \frac{0.467}{\gamma^*} \left(1 + \frac{\alpha_i}{\theta}\right)^{-1} \quad (17)$$

Figure 17 shows the variation in the stand-off distance for a plasma according to its ionization degree. The diamond points are the empirical values of Δ calculated with (10) for the applied voltages tested. The shock stand-off distance measured experimentally corresponds roughly to an ionization degree ranging from 2×10^{-5} to 2×10^{-4} . These values of α_i allow the electronic density to be calculated by considering a neutral particle density behind the shock wave of $5 \times 10^{21} \text{ m}^{-3}$. It is found that the electronic density varies between 10^{17} and 10^{18} . These values have the same order of magnitude as those mentioned in the literature for this type of discharge [3].

The increase in Δ_{exp} with the electronic density is consistent with the theoretical expression of n_e . Indeed, our measurements show that the increase of Δ_{exp} is linear with I_{HV} (section 4.2.1), which is the same type of relation as that existing between the electronic density and the current density (i.e., the discharge current I_{HV}) [43]. Further measurements will be conducted in a future study in order to access the electronic density, demonstrating experimentally the strong influence of the plasma properties on the increase in the stand-off distance.

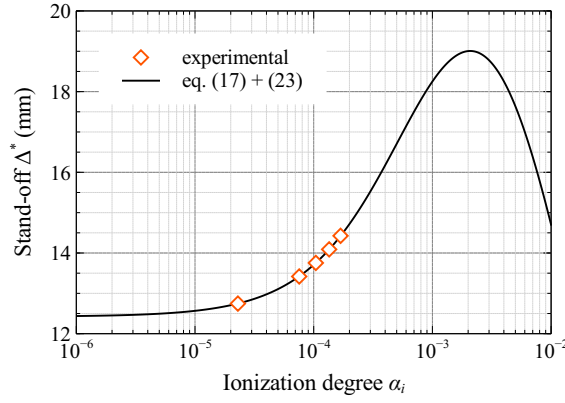


Figure 17. Stand-off distance for a plasma according to the ionization degree. The line is the theoretical variation calculated with eq. (13) and (17), and the diamonds are the empirical values calculated with eq. (10) for the applied voltages tested experimentally.

6. Conclusions

Experimental observations have shown the modification of the shock wave by the presence of a local plasma discharge. It was found that the shock wave is pushed upstream, thus increasing the detachment distance by several mm. The effect of the plasma actuator is more significant when the discharge voltage, and hence the power, is increased.

The rarefied flow field around the cylinder was numerically simulated with a 2-D Navier-Stokes code. The jump coefficients were adapted to enable application of the code in rarefied conditions, and comparisons between experiments and simulations are in agreement for natural conditions, thereby validating the approach chosen here for this geometry. Two types of heating induced by the plasma were simulated numerically. With a heating exclusively located at the electrode surface the calculations give underestimated values of the stand-off distance. These low increases were obtained with (too) high temperatures. This means that surface heating has a rather low efficiency and is not relevant here. The volumetric heating was also numerically tested and leads to opposite influence compared to those obtained with the surface heating. It was observed that a very little energy induces a marked increase in the stand-off distance. These numerical values of the detachment distance are higher than those measured experimentally and are not physically consistent. Spectroscopic measurements were performed and the rotational temperatures were estimated, showing that only a little heating occurs in the plasma volume, which is inconsistent with the numerical results. In addition, a thermal disequilibrium was measured between the dominant species N_2 and N_2^+ . These experimental observations suggest that the stand-off distance increase is not due to thermal effects and moreover as regards to the volumetric heating, since a large part of the discharge energy did not contribute to heat the flow.

Estimation of the shock wave stand-off distance with the empirical correlation of Ambrosio and Wortman was adapted to plasma conditions in which the ionization degree

and the non thermal equilibrium have been taken into account. The results show that the detachment distance increases with the ionization degree, and the comparison between numerical estimations and experiments is in good agreement. To sum up, the plasma can induce several types of effects, such as thermal heating, ionization or thermal non equilibrium. These effects have to be investigated separately in order to distinguish which one of them plays a significant role. In this study, we have demonstrated that the aerodynamic changes induced by the plasma actuator are due to the ionization rate and the thermal non equilibrium, which can only be obtained with an electric discharge. Further numerical developments will take into account a two temperature chemical kinetics in order to improve the agreement between the numerical simulations and the experimental measurements. In addition, density will be experimentally measured along the stagnation line upstream the cylinder in order to reinforce our conclusions presented in this study.

Acknowledgments

The authors gratefully acknowledge thank Nicolas Gouillon from ICARE for setting up the experiments presented in this work. Romain Jousot's fellowship is provided by the French Government's Investissement d'Avenir program: Laboratoire d'Excellence CAPRYSES (grant no. ANR-11-LABX-0006-01). Additional funding is provided by the Région Centre with the PASS grant.

References

- [1] V E Semenov, V G Bondarenko, V B Gildenburg, V M Gubchenko, and A I Smirnov. Weakly ionized plasmas in aerospace applications. *Plasma Phys. Control. Fusion*, 44(12B):B293–B305, 2002.
- [2] V M Fomin, P K Tretyakov, and J-P Taran. Flow control using various plasma and aerodynamics approaches (short review). *Aerosp. Sci. Technol.*, 8(5):411–21, 2004.
- [3] P Bletzinger, B N Ganguly, D van Wie, and A Garscadden. Plasmas in high speed aerodynamics. *J. Phys. D: Appl. Phys.*, 38(4):R33–R57, 2005.
- [4] E Moreau. Airflow control by non-thermal plasma actuators. *J. Phys. D: Appl. Phys.*, 40(3):605–36, 2007.
- [5] T C Corke, C L Enloe, and S P Wilkinson. Dielectric barrier discharge plasma actuators for flow control. *Annu. Rev. Fluid Mech.*, 42(1):505–29, 2010.
- [6] L N Cattafesta III and M Sheplak. Actuators for active flow control. *Annu. Rev. Fluid Mech.*, 43(1):247–272, 2001.
- [7] L Wang, Z B Luo, Z X Xia, B Liu, and X Deng. Review of actuators for high speed active flow control. *Sci. China Tech. Sci.*, 55(8):2225–2240, 2012.
- [8] J Menart, J Shang, C Atzbach, S Magoteaux, and M Slagel. Total drag and lift measurements in a mach 5 flow affected by a plasma discharge and a magnetic field. In *AIAA Paper No. 2005–947*, 2005.
- [9] G I Mishin, Y L Serov, and I P Yavor. Flow around a sphere moving supersonically in a gas discharge plasma. *Sov. Tech. Phys. Lett.*, 17(6):413–6, 1991.
- [10] M Samimy, I Adamovich, B Webb, J Kastner, J Hileman, S Keshav, and P Palm. Development

- and characterization of plasma actuators for high-speed jet control. *Exp. Fluids*, 37(4):577–88, 2004.
- [11] S B Leonov, D A Yarantsev, V G Gromov, and A P Kuriachy. Mechanisms of flow control by near-surface electrical discharge generation. In *AIAA Paper No. 2005-780*, 2005.
 - [12] S B Leonov, V N Sermanov, V R Soloviev, and D A Yarantsev. Supersonic rupture's shock control by electrical discharge. In *New Trends in Fluid Mechanics Research, Proceedings of the Fifth International Conference on Fluid Mechanics (Shanghai, 2007)*. Springer-Verlag, Berlin Heidelberg, 2009.
 - [13] A Klimov, V Bityurin, and Y Serov. Non-thermal approach in plasma aerodynamics. In *AIAA Paper No. 2001-0348*, 2001.
 - [14] V A Bityurin and A I Klimov. Non-thermal plasma aerodynamics effects. In *AIAA Paper No. 2005-978*, 2005.
 - [15] E Menier, L Leger, E Depussay, V Lago, and G Artana. Effect of a dc discharge on the supersonic rarefied air flow over a flat plate. *J. Phys. D: Appl. Phys.*, 40(3):695–701, 2007.
 - [16] J-D Parisse, L Léger, E Depussay, V Lago, and Y Burtshell. Comparison between mach 2 rarefied airflow modification by an electrical discharge and numerical simulation of airflow modification by surface heating. *Phys. Fluids*, 21(10):106103, 2009.
 - [17] L H Townend. Research and design for lifting reentry. *Prog.Aerosp. Sci.*, 19(1):1–80, 1979.
 - [18] E H Hirschel. *Basics of Aerothermodynamics*. Springer-Verlag, Berlin Heidelberg, 2005.
 - [19] P Baiocco, S Guedron, P Plotard, and J Moulin. The Pre-X atmospheric re-entry experimental lifting body: Program status and system synthesis. *Acta Astronaut.*, 61(1):459–74, 2007.
 - [20] G Pezzella, G Marino, and G C Rufolo. Aerodynamic database development of the ESA intermediate experimental vehicle. *Acta Astronaut.*, 94(1):57–72, 2014.
 - [21] J S Shang, S T Surzhikov, R Kimmel, D Gaitonde, J Menart, and J Hayes. Mechanisms of plasma actuators for hypersonic flow control. *Prog.Aerosp. Sci.*, 41(8):642–68, 2005.
 - [22] J Allegre. The SR3 low density wind-tunnel. Facility capabilities and research development. In *AIAA Paper No. 92-3972*, 1992.
 - [23] NOAA, NASA, and US Air Force. U.S. standard atmosphere. Technical Report NASA-TM-X-74335, National Aeronautics and Space Administration (NASA), US Government Printing Office, Washington DC, 1976.
 - [24] M Gad-el-Hak. The fluid mechanics of microdevices - the Freeman scholar lecture. *J. Fluid. Eng.-T. ASME*, 121(1):5–33, 1999.
 - [25] V V Riabov. Numerical simulation of rarefied-gas flows about a rotating cylinder. In *Rarefied Gas Dynamics. Proceedings of the 25th Symposium on Rarefied Gas Dynamics, St.-Petersburg, Russia (pp. 777-783)*, 2006.
 - [26] M Y Plotnikov and A K Rebrov. Relaxation processes in hypersonic rarefied binary gas mixture flow around a cylinder. *Fluid Dyn.*, 43(3):493–502, 2008.
 - [27] T J Scanlon, E Roohi, C White, M Darbandi, and J M Reese. An open source, parallel DSMC code for rarefied gas flows in arbitrary geometries. *Comput. Fluids*, 39(10):2078–89, 2010.
 - [28] K Morinishi. A continuum/kinetic hybrid approach for multiscale flow simulation. In *European Conference on Computational Fluid Dynamics ECCOMAS CFD (Vol. 1, No. 0.8, pp. 0-6)*, 2006.
 - [29] A J Lofthouse, L C Scalabrin, and I D Boyd. Velocity slip and temperature jump in hypersonic aerothermodynamics. *J. Thermophys. Heat Tr.*, 22(1):38–49, 2008.
 - [30] G N Markelov, A N Kudryavtsev, and M S Ivanov. Continuum and kinetic simulation of laminar separated flow at hypersonic speeds. *J. Spacecraft Rockets*, 37(4):499–506, 2000.
 - [31] J O Hirschfelder, C F Curtiss, and R B Bird. *Molecular Theory of Gases and Liquids*. Wiley, New York, 1954.
 - [32] M W Chase, C A Davies, J R Downey, D J Frurip, R A McDonald, and A N Syverud. Janaf thermochemical tables, third edition. *J. Phys. Chem. Ref. Data*, 14(Suppl. 1):1–1856, 1985.
 - [33] M N Kogan. *Rarefied Gas Dynamics*. Plenum Press, New York, 1969.
 - [34] F Sharipov. Data on the velocity slip and temperature jump coefficients [gas mass, heat and

- momentum transfer]. In *Proceedings of the 5th International Conference on Thermal and Mechanical Simulation and Experiments in Microelectronics and Microsystems, EuroSimE 2004*, pages 243–9, 2004.
- [35] M von Smoluchowski. Ueber wärmeleitung in verdünnten gasen. *Ann. Phys.-Berlin*, 300(1):101–30, 1898.
- [36] E Kennard. *Kinetic Theory of Gases*. McGraw-Hill, New York, 1938.
- [37] F Sharipov. Application of the cercignanilampis scattering kernel to calculations of rarefied gas flows. II. Slip and jump coefficients. *Eur. J. Mech. B-Fluids*, 22(2):133–43, 2003.
- [38] G A Bird. *Molecular Gas Dynamics and the Direct Simulation of Gas Flows*. Oxford University Press, New York, 1994.
- [39] E S Moulic. Afterglow investigations of shock detachment distances at low reynolds numbers. Technical Report WADC technical report, 57-643, Wright Air Development Center, Armour Research Foundation of Illinois Institute of Technology, 1958.
- [40] F S Billig. Shock-wave shape around spherical- and cylindrical-nosed body. *J. Spacecraft Rockets*, 4(6):822–3, 1967.
- [41] A Ambrosio and A Wortman. Stagnation point shock detachment distance for flow around spheres and cylinders. *ARS J.*, 32(2):281, 1962.
- [42] C A Schneider, W S Rasband, and K W Eliceiri. Nih image to imagej: 25 years of image analysis. *Nat. Methods*, 9(7):671–5, 2012.
- [43] Y P Raizer. *Gas discharge Physics*. Springer-Verlag, Berlin Heidelberg, 1991.
- [44] J C Lengrand. *Mesure des températures de rotation dans l’azote à basse densité par sonde à faisceau électronique. Application à l’étude des écoulements*. PhD thesis, Université Paris VI, France, 1974.
- [45] P Laborie, J M Rocard, and J A Rees. *Electronic cross-sections and macroscopic coefficients - Metallic vapours and molecular gases*. Dunod, Paris, 1971.
- [46] V Lago. *Mesure des températures électroniques et rotationnelles dans des jets supersoniques de plasmas d’air et d’azote*. PhD thesis, Université Paris Sud, France, 1993.
- [47] S O Macheret, M N Shneider, and R B Miles. Magnetohydrodynamic control of hypersonic flows and scramjet inlets using electron beam ionization. *AIAA J.*, 40(1):74–81, 2002.
- [48] W D Hayes and R F Probstein. *Hypersonic flow theory, Vol. I Inviscid flows*. Academic Press, New York, 1966.
- [49] M D Van Dyke. The supersonic blunt-body problem - Review and extension. *J. Aero. Sci.*, 25(8):485–496, 1958.
- [50] H Lowry, C Stepanek, L Crosswy, P Sherrouse, M Smith, L Price, W Ruyten, and J Felderman. Shock structure of a spherical projectile in weakly ionized air. In *AIAA Paper No. 1999-0600*, 1999.
- [51] R N Schwartz and J Eckerman. Shock location in front of a sphere as a measure of real gas effects. *J. Appl. Phys.*, 27(2):169–74, 1956.
- [52] Y Ishida, T Idehara, and T Noda. Observation of anomalous sound velocity in weakly ionized plasma. *Phys. Lett.*, 36A(4):273–4, 1971.
- [53] G I Mishin. Equation of state for a weakly ionized gas-discharge plasma. *Tech. Phys. Lett.*, 23(7):570–2, 1997.
- [54] K T A L Burm, W J Goedheer, and D C Schram. The isentropic exponent in plasmas. *Phys. Plasmas*, 6(6):2622–7, 1999.
- [55] J D Anderson Jr. *Fundamentals of Aerodynamics, third edition*. McGraw-Hill, New York, 2001.
- [56] K T A L Burm, W J Goedheer, and D C Schram. Mach numbers for gases and plasmas in a convergent-divergent cascaded arc. *Phys. Plasmas*, 6(6):2628–35, 1999.